DOI: 10.13009/EUCASS2023-382
Aerospace Europe Conference 2023 – 10TH EUCASS – 9TH CEAS

Hypervelocity impact simulations between space objects with various shapes and lattice core sandwich panel

Mi Jang, Hyun-Cheol Shin** and Jae-Sang Park*†*

** Chungnam National University, 34134 Daejeon, Republic of Korea*
mij8666@o.cnu.ac.kr
aerotor@cnu.ac.kr
*** Hanwha Systems, 17121 Yongin, Republic of Korea*
hcshin1066@hanwha.com
† Corresponding Author

Abstract
This study conducts the hypervelocity impact (HVI) simulations between space objects with different shapes and lattice core sandwich panels (LCSP). A commercial nonlinear structural dynamic analysis code, LS-DYNA, is used for the present HVI analysis. Mie-Gruneisen equation of state and Johnson-Cook material strength and failure models are used to represent the hydrodynamic and nonlinear structural behaviors of metallic materials. The shape effects of the space objects on the HVI behaviors are investigated for the LCSP structure. Disk space objects are found to be the most damaging shape among sphere, cube, and cylinder.

1. Introduction

Since the beginning of space age, the amount of space debris in Earth's orbit has been continuously increasing. Figure 1 shows the number of cases of satellite fragmentation by year. From 2001 to 2021, there were an average of five cases of satellite breakups per year, resulting in a large amount of space debris. Furthermore, with the transition to the New Space Era, the paradigm of space development has shifted to micro satellites and satellite constellations, leading to a rapid increase in the number of space objects. As the Earth's orbit becomes more crowded, the risk of satellite collisions also increases. In the past 10 years, the number of collisions between space objects has increased by 3% compared to accidents between space objects since human space development [1]. However, small space debris, less than a centimeter in size, is difficult to detect and avoid; therefore, collisions between space debris and space structures can occur. As of March 2023, it is estimated that there are 130 million small space debris with centimeter size in Earth's orbit [1]. Collisions with Micrometeoroids and Orbital Debris (MMOD) occur at orbital velocities typically exceeding 7 km/s, which is considered as the hypervelocity impact (HVI) behavior. Even very small MMOD can damage critical components such as electronics, causing a spacecraft or satellite to malfunction or be destroyed. Figure 2 shows the craters and pits created by the collision between the reaction control system engine nozzle of the SpaceX Crew-4 vehicle and the MMOD. 14 MMOD impact damage is known to have occurred during a SpaceX Crew-4 mission to the docking part of the ISS [2]. Thus, the shielding systems are required to protect space structures from collision risks with space debris.

In 1947, the Whipple shielding system was invented to protect space structures [3]. The simplest Whipple shield consists of a bumper and a rear wall separated by a certain distance, shown in Fig. 3. The debris cloud generated by HVI between the collision object and the bumper diffuses as far as the standoff distance, dispersing and mitigating the impact energy applied to the rear wall to protect space structures [3]. Single-purpose shields such as Whipple shields are installed on the outer walls of space structures and cause an increase in the installation volume and total mass. They are mainly used for manned space structures such as space stations [4]. Weight efficiency is one of the leading design criteria in space structure design. Therefore, for unmanned satellites, multi-purpose shields with sandwich panel structures with good weight efficiency are used than Whipple protection systems [5]. The honeycomb sandwich panel (HCSP) is a representative example used for the outer wall of the satellite's bus structure, withstanding launch loads and performing shock-absorbing against MMOD [6]. However, due to the channeling effect, honeycomb cores can have reduced protection performance. The debris cloud generated by HVI with space debris cannot spread widely but moves along the cell walls of the honeycomb cores, concentrating impact energy and momentum on small areas of rear plates [7]. Various studies had been conducted to improve the shielding capability of sandwich panels by changing the

DOI: 10.13009/EUCASS2023-382

material of bumpers or rear walls [8, 9] or the topology of cores [10, 11]. Among different core designs, lattice core structures have high stiffness and strength at low density and impact energy absorption advantages, allowing lightweight design [12]. They are attracting attention as an alternative to honeycomb structures [13]. In addition, open-cell structures such as lattice truss cores are suitable for multi-purpose applications combining thermal and structural functions [14, 15]. HVI experiments were performed on monolithic plates and pyramidal lattice core sandwich panels (LCSP), suggesting that sandwich plates surpass monolithic plates for multi-functional applications that require structural efficiency with ballistic performance [14]. HVI experiments using a two-stage light gas gun were carried out on different types of sandwich panels, such as honeycomb and lattice cores [16]. Previous studies were conducted experimentally using spherical projectiles, but most space objects in the actual space environment are non-spherical. Ballistic performance varies depending on the geometry of the space object. Multiple studies have shown that non-spherical objects can be more destructive than spherical ones [17-19]. However, no studies have been carried out on the different shapes of space objects in the HVI on the LCSP.

Therefore, in this study performs HVI simulations between LCSP space structures and different shapes of space objects using numerical analysis. The simulations are conducted using LS-DYNA, a commercial non-linear structural dynamics analysis solver. For space objects with different shapes and identical mass, the geometries of sphere, cube, cylinder, and disk are considered. The final damage shape of the structure is investigated through HVI simulations to evaluate the shielding performance of LCSP with various space objects.

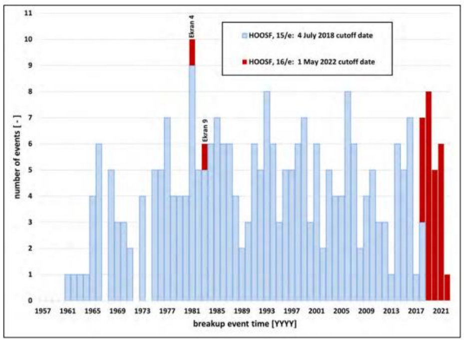

Figure 1: Number of satellite breakups by year since 1961 [1]

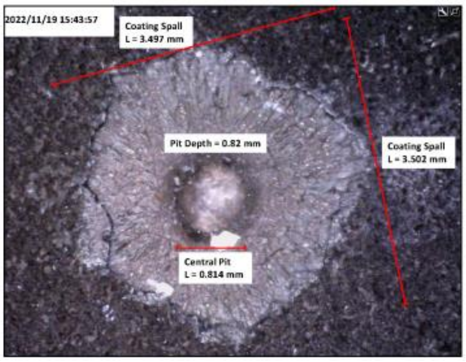

Figure 2: Impact feature observed on reaction system engine nozzle of the Crew-4 vehicle [2]

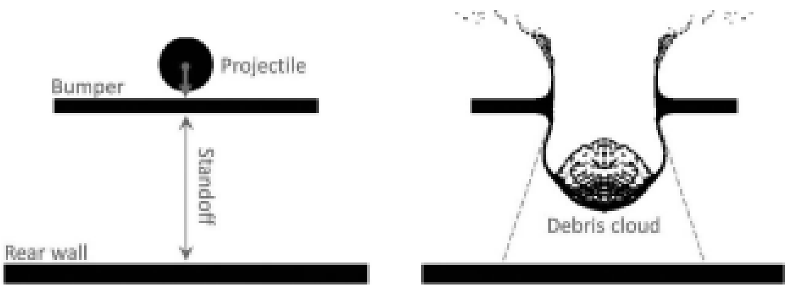

Figure 3: Schematic of a Whipple shield design principle [5]

DOI: 10.13009/EUCASS2023-382

2. Simulation methods

In this study, LS-DYNA, a commercial hydrocode, is used and nonlinear structural dynamic analyses based on the explicit scheme are conducted for HVI simulations. The hydrocode consists of equations of state, constitutive equations, and failure models. In addition, the conservations of mass, momentum and energy are applied to solve the problems. The techniques and modeling methods used in the simulation are described below.

2.1 Smoothed particle hydrodynamic (SPH)

SPH is a mesh-free method that discretizes the continuum into a finite number of particle elements. This technique can represent problems that undergo large deformations, such as collisions or explosions, without distortion or entanglement of the elements. In particular, it is widely used in the numerical analysis of hypervelocity impacts because it can realistically realize the dispersion phenomenon of debris clouds [20]. Physical quantities such as the position and mass of each particle are approximated by a kernel function using Equation (1).

$$\langle f(x)\rangle = \sum_{j=1}^{N} \frac{m_j}{\rho_j} f(x_j) W(x - x_j, h) \tag{1}$$

where N is the number of particles and $f(x_j)$ is the state quantity at the position of the j-th particle. W is the kernel function represented in terms of the distance between two particles $(x - x_j)$ and the smoothing length (h) defining the influence region for approximation. The cubic B-spline kernel function is the most commonly used (Equation (2))

$$W(q,h) = \alpha \times \begin{Bmatrix} 1 - \frac{3}{2}q^2 + \frac{3}{4}q^3 & 0 \le q \le 1 \\ \frac{1}{4}(2-q)^3 & 1 \le q \le 2 \\ 0 & q \ge 2 \end{Bmatrix} \tag{2}$$

where q can be expressed as $q = (|x - x_j|)/h$, and α is a normalization constant that depends on the number of space dimensions. In one, two, and three dimensions, $\alpha = 2/3h$, $10/7\pi h^2$, and $1/\pi h^3$, respectively [21].

The SPH governing equation consists of a continuity equation, a momentum conservation equation, and an energy conservation equation. Substituting the SPH approximations for a function and derivatives into the governing equations can be written as Equations (3) to (5)

$$\frac{d}{dt}\rho_i = -\rho_i \sum_j \frac{m_j}{\rho_j}(v_j - v_i)A_{ij} \tag{3}$$

$$\frac{d}{dt}v_i = \sum_j m_j \left(\frac{\sigma_i}{\rho_i^2}A_{ij} - \frac{\sigma_j}{\rho_j^2}A_{ji}\right) \tag{4}$$

$$\frac{d}{dt}e_i = \frac{P_i}{\rho_i^2} \sum_j m_j (v_j - v_i) A_{ij} \tag{5}$$

In these equations, the symbols, ρ_i, v_i, and e_i, indicate particle density, velocity, and internal energy, respectively. σ_i is the Cauchy stress, m_i is the mass of the particle, and A_{ij} is the gradient of the kernel function defined by Equation (6) [22].

$$A_{ij} = \frac{\partial}{\partial x_i} W(x - x_j, h) \tag{6}$$

In order to prevent non-physical phenomena that may occur due to numerical instability in hypervelocity impact simulations, the artificial viscosity Π_{ij} is added to a momentum and energy conservation equation [23]. The artificial viscosity term is evaluated as Equation (7)

DOI: 10.13009/EUCASS2023-382

$$\Pi_{ij} = \begin{cases} \dfrac{-\alpha\mu_{ij}\bar{c} + \beta\mu_{ij}^2}{\bar{\rho}} & if\ v_{ij}r_{ij} < 0 \\ 0 & otherwise \end{cases} \tag{7}$$

where α and β are constants determining the magnitude of virtual viscosity, $\bar{c}$ is an adiabatic sound speed, and μ_{ij} is a pseudo-artificial pressure term [24, 25].

2.2 Equation of state (EOS)

When a solid material is subjected to a high pressure that exceeds the yield strength of the material, the material behaves like a fluid at a high strain rate. The hydrodynamic behavior of materials can be described using an equation of state (EOS), representing the relationship between the hydrostatic pressure, the local density, and the local specific energy [26]. The equation of state can be expressed in different ways depending on the thermodynamic properties of the material and is used to describe the volume compression or expansion behavior of various materials [27]. Among these, the Mie-Gruneisen equation of state is known to be suitable for metallic materials subjected to high-speed impact loadings [24]. The Mie-Gruneisen equation of state then defines the pressure for compressed materials as given in Equation (8)

$$P = \frac{\rho_0 C_0^2 \mu \left[1 + \left(1 - \frac{\gamma_0}{2}\right)\mu - \frac{a}{2}\mu^2\right]}{\left[1 - (S_1 - 1)\mu - S_2\dfrac{\mu^2}{(\mu+1)} - S_3\dfrac{\mu^3}{(\mu+1)^2}\right]^2} + (\gamma_0 + a\mu)E \tag{8}$$

and for expanded materials as shown in Equation (9)

$$P = \rho_0 C_0^2 \mu + (\gamma_0 + a\mu)E \tag{9}$$

where C_0 is the speed of sound in material, S_1, S_2, and S_3 are the slope coefficients of the shock velocity-particle velocity (u_s-u_p) curve, γ_0 is the Gruneisen gamma, a is the first-order volume correction factor, $\mu = (\rho/\rho_0 - 1)$ is compression ratio, and E denotes the internal energy per initial volume [25]. Table 1 presents the values for the EOS input parameters of the materials used in the simulations.

Table 1: Equation of state parameters used in simulations [26]

Material	**C_0 (mm/ms)**	**ρ_0 (g/cm^3)**	**S_1**	**γ_0**
Al2017-T4	5328	2.780	1.338	2.000
Al5052	5240	2.680	1.340	2.000
Al6061-T6	5240	2.703	1.400	1.970

2.3 Material strength and failure model

Even if the problem is calculated using the hydrodynamic equation of state, in the case of a hypervelocity impact problem, the material strength must be considered at a point far from the point of impact or at a point that is considerably past the point of impact [20] thesis. Solid materials undergo plastic deformations under extreme impact loads that exceed the yield strength of the material, such as collisions and explosions. A material strength model can be used to describe the nonlinear elastic-plastic response of a material. Several types of material strength models depend on the expression of the material response to loads. In this study, the Johnson-Cook strength model is used, which represents the dynamic behavior of materials taking into account high strain, high strain rate, and temperature

DOI: 10.13009/EUCASS2023-382

effects in hypervelocity impacts [28]. This model is widely used in the numerical simulation of hypervelocity impact. The flow stress is defined by Equations (10) and (11) [29].

$$\sigma = (A + B\varepsilon^n)(1 + C \ln \dot{\varepsilon}^*)(1 - T^{*m}) \tag{10}$$

Where

$$T^* = \frac{T - T_{ref}}{T_{melt} - T_{ref}} \tag{11}$$

The first bracket on the right of the Equation (10) reflects the strain rate, the second is for the strain rate, and the third is the effect of temperature. A, B, C, n, and m are material constants indicating yield strength, hardening constant, strain rate constant, strain hardening exponent, and thermal softening exponent, respectively. ε is the equivalent plastic strain, $\dot{\varepsilon}^*$ is the dimensionless equivalent plastic strain rate, T^* is the homologous temperature, T_{melt} is the melting temperature of the material, and T_{ref} is room temperature.
In the Johnson-Cook failure model, the damage to an element is defined by the Equation (12), and failure occurs when the damage parameter D reaches the value of 1 [25, 29].

$$\mathrm{D} = \sum \frac{\Delta\varepsilon}{\varepsilon^f} \tag{12}$$

where $\triangle\varepsilon$ is the increment of equivalent plastic strain during the integration cycle, and ε^f is the equivalent strain to fracture under the current strain rate, temperature, pressure, and equivalent stress conditions. The strain at fracture is given by Equations (13) and (14)

$$\varepsilon^f = (D_1 + D_2 e^{1.5D_3})(1 + D_4 \ln \dot{\varepsilon}^*)(1 + D_5 \mathrm{T}^*)\ where\ \sigma^* > 1.5 \tag{13}$$

$$\varepsilon_P^f = \left(D_1 + D_2 e^{D_3\sigma^*}\right)(1 + D_4 \ln \dot{\varepsilon}^*)(1 + D_5 t^*)\ where\ \sigma^* \leq 1.5 \tag{14}$$

where D_1 to D_5 are the coefficients in the Johnson-Cook damage model and σ^* is the dimensionless pressure-stress ratio. The material model parameters used in the simulations are given in Table 2.

Table 2: Johnson-Cook model parameters used in simulations [30-32]

Material	A (MPa)	B (MPa)	n	C	m	D_1	D_2	D_3	D_4	D_5
Al2017-T4	369	684	0.73	0.0083	1.70	0.1120	0.1230	1.5000	0.0070	0
Al5052	143	215	0.54	0.0046	0.90	0.3060	0.0446	-1.7200	0.0056	0
Al6061-T6	324	114	0.42	0.0020	1.34	-0.7700	1.4500	-0.4700	0	1.6000

2.4 Numerical models

In this study, an HVI simulation is conducted between various space objects and space structures. The space object collides with the space structure at 6.72 km/s under normal impact conditions without incidence angle, and the entire simulation is performed during 40 μs. Four different shapes are considered for space objects and Al2017-T4 is used as the structural material (Figure 4). The space structure consists of a front wall, a core, and a rear wall. The front and rear walls are designed using Al6061-T6 with dimensions of 30 mm × 30 mm and a thickness of 1 mm. A core is inserted between the two panels, and a honeycomb structure and a lattice structure are considered. The structural material for the two types of the core is Al5052. The detailed modeling method for each part is explained below.

DOI: 10.13009/EUCASS2023-382

2.4.1 Space objects

Four different shapes are considered for space objects in this HVI simulation to the LCSP space structure: a sphere, a cube, a cylinder, and a disk. Space objects are characterized by the diameter (D) and length (L) along the impact direction. A shape with a larger L/D ratio is defined as a long object, and that with a smaller L/D ratio is defined as a short object, and both L/D ratios are considered for cylinder and disk configurations. All space objects are designed with a mass of 0.012 g to consider only the shape effect. Since the space object is completely disintegrated and formed into a debris cloud by the high-speed collision with the space structure, it is modeled using the SPH technique, and the distance between particles is uniformly assumed to be 0.1 mm in all directions. Figure 4 shows the modeling information of various shapes of space objects used in this study.

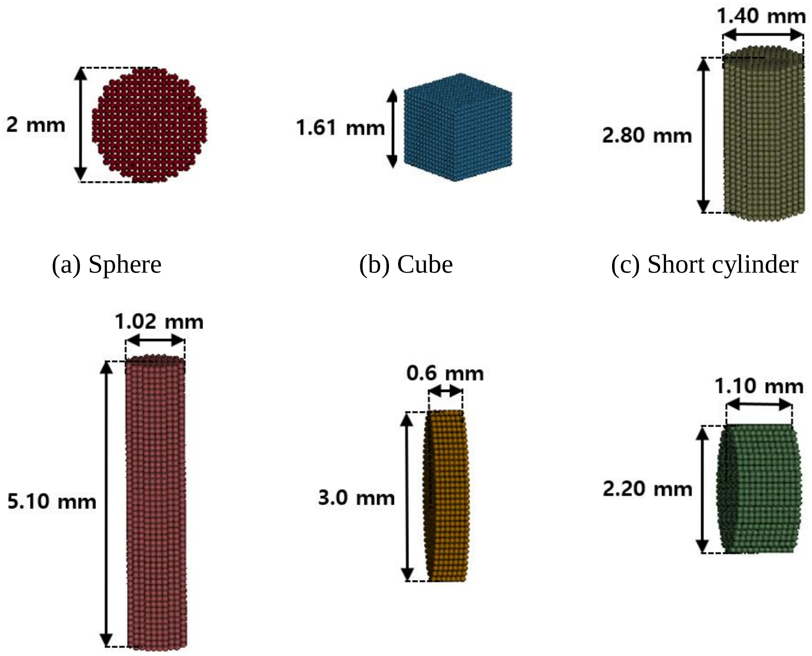

(a) Sphere (b) Cube (c) Short cylinder

(d) Long cylinder (e) Short disk (f) Long disk

Figure 4: Geometric dimensions of space objects

2.4.2 Space structure – front wall

In the case of hypervelocity impact, local deformation occurs only at a location very close to the impact location. Therefore, the front wall (Figure 5) where a direct collision with a space object occurs is composed of a direct impact area and an indirect impact area and the edges of the space structure are applied to fixed boundary condition. The diameter of the direct impact area is 20 mm, and since a collision with a space object results in a high deformation, it is modeled with SPH technique. The distance between SPH particles is set to 0.1 mm, which is the same value used in the modeling of a space object, and 314 280 particles are used. The indirect collision area is represented by FEM technique using 3 600 3D solid elements for computational efficiency. The two areas are connected using *CONTACT_TIED_NODES_TO_SURFACE algorithm in LS-DYNA.

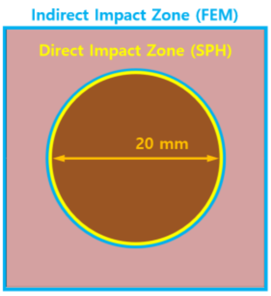

Figure 5: Top view of the space structure (Front wall)

DOI: 10.13009/EUCASS2023-382

2.4.3 Space structure – core

This paper considers two types of cores such as the honeycomb core (Figure 6(a)) and the lattice core (Figure 6(b)). The thickness of the honeycomb core is 33 mm, and using the cell given in Figure 7(a). Since the thickness of the honeycomb cell is very thin at 0.0762 mm in the single wall, it is modeled using 131 008 2D shell elements. The contact between the debris cloud's SPH particles and the honeycomb core's shell element is expressed using the *CONTACT_AUTOMAITC_NODES_ TO_SURFACE algorithm in LS-DYNA. The lattice core is designed with the same weight (7.2 g) as the honeycomb core by adjusting the thickness of the core to 20 mm. A unit cell of the body-centered cubic structure (Figure 7(b)) is used, and the total lattice core is modeled using 617 650 SPH particles.

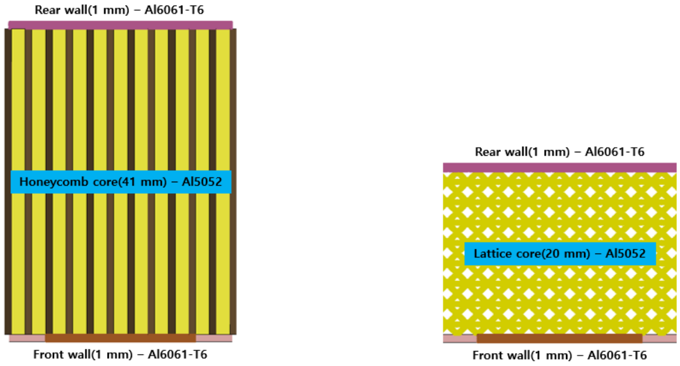

(a) Honeycomb core sandwich panel (b) Lattice core sandwich panel

Figure 6: Sectioned view of the space structure

(a) Honeycomb cell (b) BCC unit cell

Figure 7: Dimension of cell

2.4.4 Space structure – rear wall

The rear wall (Figure 8) is modeled with *ADAPTIVE_SOLID_TO_SPH in LS-DYNA, which is a hybrid FEM/SPH technique to consider the different damage levels of rear walls from the small deformations to substantial structural deformations by the debris cloud [17]. The hybrid FEM/SPH technique converts extreme distortions in FEM elements to SPH elements. SPH elements replace the failed solid Lagrangian elements inheriting all the Lagrange nodal quantities and all the Lagrange integration points [33]. The interaction between the debris cloud's SPH particles and the rear wall's solid element is implemented using *CONTACT_ERODING_NODES_TO_SURFACE in LS-DYNA.

Figure 8: Rear view of the space structure (Rear wall)

DOI: 10.13009/EUCASS2023-382

3. Numerical results and discussion

3.1 Validation of the HVI simulation method

A comparison study between the present analysis and the previous HVI test [34] is conducted to validate the HVI simulation techniques. In this HVI example, an aluminium sphere and a thin aluminium plate are considered. A schematic diagram for this validation study is shown in Figure 9. Al2017-T4 and Al6061-T6 are used for the projectile and thin plate, respectively. A spherical projectile with a diameter of 9.53 mm collides with a 0.968 mm thick plate at 6.72 km/s.

The projectile is modeled by the SPH technique. As described in Section 2.4.2, the direct impact area of the space structure is represented by the SPH method, and the indirect impact area is modeled as the FEM method using solid elements. Mie-Gruneisen and Johnson-Cook models represent the behaviors of Al2017-T4 and Al6061-T6. EOS and material model parameters for Al2024-T3 instead of Al2017-T4 are used considering the metallurgical proximity since the parameters for Al2017-T4 are not available [26]. If the distance between particles is not small enough, inaccurate results may be obtained [35]. Therefore, a convergence study is performed to find the distance between particles that can adequately describe the debris cloud.

The prediction results using difference SPH particle distances are compared with the measured data for the debris cloud configuration at t=7.3 μs. Figure 10 represents the criteria for definition of the geometry of debris cloud. The length L from the back of the plate to the front of the debris cloud, the maximum radius R of the debris cloud, and the axial velocity V at the front of the debris cloud are used when validating the debris cloud from HVI. As seen in Figure 11, the debris clouds from the present analysis and the previous test [34] are quite similar. Figure 12 and Table 3 show the errors in geometry and velocity of the debris cloud when different SPH particle distances are considered. The maximum error within 5% can be achieved when the distance between the particles is 0.1mm. Therefore, the present modeling and analysis techniques are well validated for the HVI simuations.

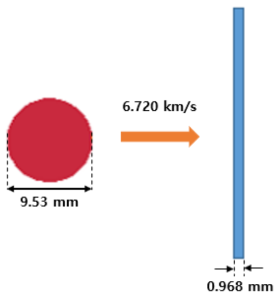

Figure 9: Schematic diagram of HVI on a thin plate

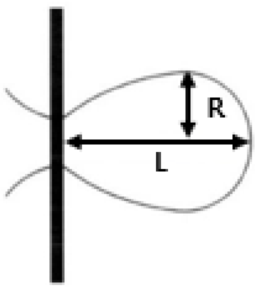

Figure 10: Geometric parameters of debris cloud

DOI: 10.13009/EUCASS2023-382

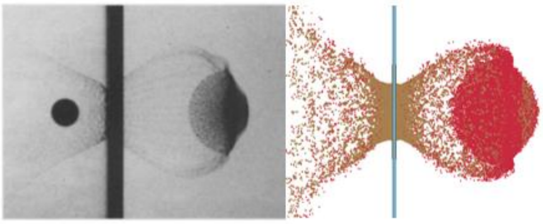

Figure 11: Comparison of debris between experiment [34] (Left) and present (Right, LS-DYNA)

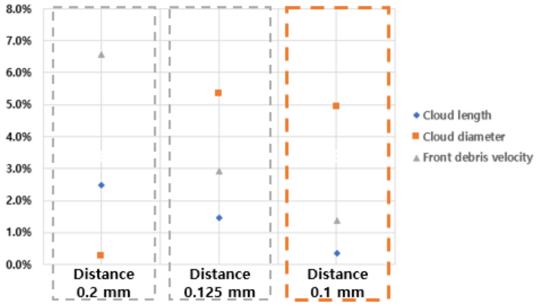

Figure 12: Diagram of error in each measured parameter in terms of SPH particle distance

Table 3: Comparison of geometry and velocity of debris cloud [23, 34]

Particle Distance [mm]	L [mm]	Relative Error (%)	R [mm]	Relative Error (%)	V [mm/µs]	Relative Error (%)
0.200	48.88	2.47	22.36	0.27	6.97	6.57
0.125	48.40	1.47	23.49	5.34	6.73	2.91
0.100	47.54	-0.34	23.40	4.93	6.63	1.38
Test 4-1283	47.7	N/A	22.3	N/A	6.54	N/A

3.2 HVI simulations

In this section, the HVI simulations are performed considering different shapes of space objects, and the shielding performance of space structures such as HCSP and LCSP is investigated by comparing the damage of the rear wall. As discussed in Section 2.4.1, the four space objects with sphere, cube, cylinder, and disk are considered. The space object collides with the space structure in a normal direction at 6.72 km/s. The total simulation time in this study is set to 40 µs.

The HVI simulation results are given in Figure 13 when the sphere collides with the HCSP structure. As shown in Figure 13(a), the debris cloud generated by interactions with the space object and front wall is not widely dispersed and but concentrated with the channelling effect at t=8µs. Consequently, the impact energy focuses on a small area, resulting in the rear wall's perforation and generating numerous holes (Figure 13(b)). The total area of the hole is 27.58 mm^2. Figure 14 shows the HVI simulation between the spherical space object and the LCSP structure. In contrast to the HCSP in Figure 13, the multi-shock effect is observed in which the debris cloud collides with the strut of the lattice core several times and expands over a wide area (Figure 14(a)). Due to the diffusion of the debris cloud, the impact energy is diminished, resulting in only small deformations of the rear wall (Figure 14(b)). As a result, LCSP has better ballistic resistance performance than HCSP against the spherical space object.

Other space objects with different shapes such as the cube, cylinder, and disk in Figure 4 are considered for the HVI simulation against the LCSP structure in order to investigate the effect of the space object configuration on the shielding performance of the LCSP structure. Figure 15(a) indicates that when the cubic space object collides with the LCSP, at t = 8 µs, the debris cloud does not spread uniformly but in two directions. As a result, only bulges of the rear wall are observed as seen in Figure 15(b), similar to the previous results for the spherical space object. Figure 16 presents the

DOI: 10.13009/EUCASS2023-382

HVI simulation using the short cylinder. Unlike the cubic space object, the debris at t = 8 μs spreads uniformly, and no damage occurs to the outer rear wall. In the case of the HVI simulation using the long cylinder, the damage is increased compared to the result using the short cylinder, and large deformations are generated, but the rear wall is not perforated (Figure 17). The simulation result of the short disk is given in Figure 18. The collision with the front wall disintegrates the space object, forming an inner cone as indicated by the blue dotted line at t = 3 μs. This phenomenon is caused by the spallation in the space structure due to the impact with the large cross-sectional area of the disk [36]. Similar to results for the cube, the debris cloud by the short disk spreads in two directions; however, the perforation of the rear wall occurs. The failure area is 3.83 mm^2. Finally, Figure 19 shows the simulation results with the long disk. Two holes are generated and the total area of the hole is 1.61 mm^2, which is approximately 58% less than the result using the short disk.
Table 4 summarizes the HCSP and LCSP rear wall hole sizes when different shaped space objects are used for the present HVI simulations. For the spherical space object, HCSP generates many holes on the rear wall, except for the LCSP with the same mass. Among space objects of different shapes, LCSP perforation occurs only for the case with the disk shape, and of these, the most significant damage occurs in the short disk.

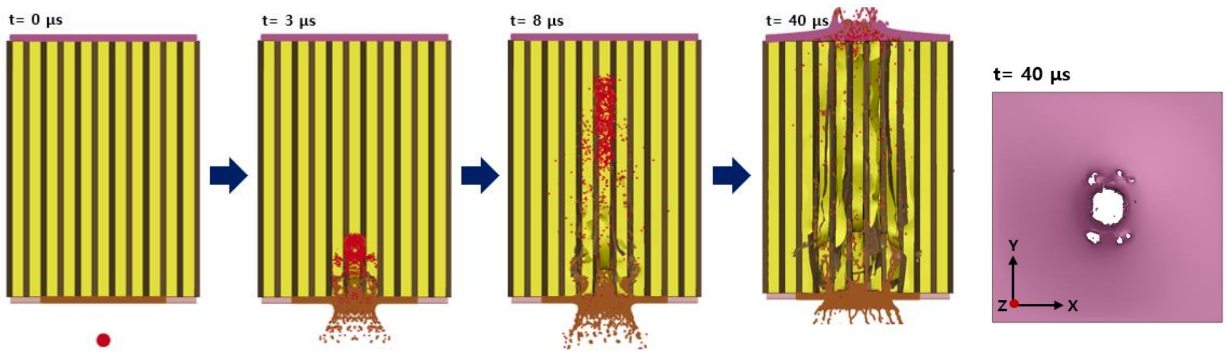

(a) Sectioned view (b) Rear view

Figure 13: HVI simulation result between Honeycomb Core Sandwich Panel (HCSP) and sphere

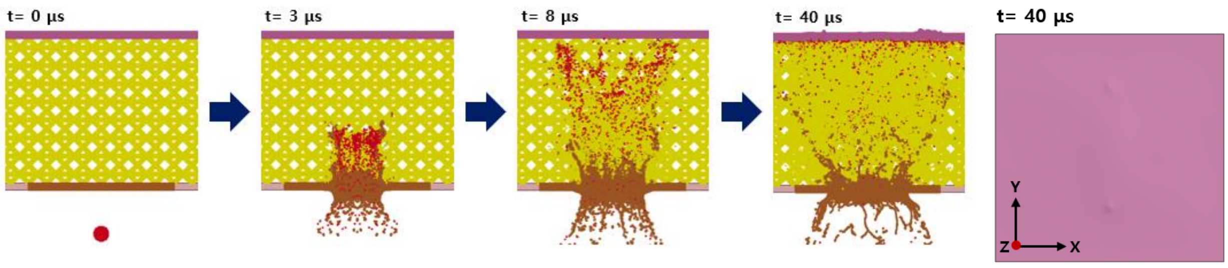

(a) Sectioned view (b) Rear view

Figure 14: HVI simulation result between Lattice Core Sandwich Panel (LCSP) and sphere

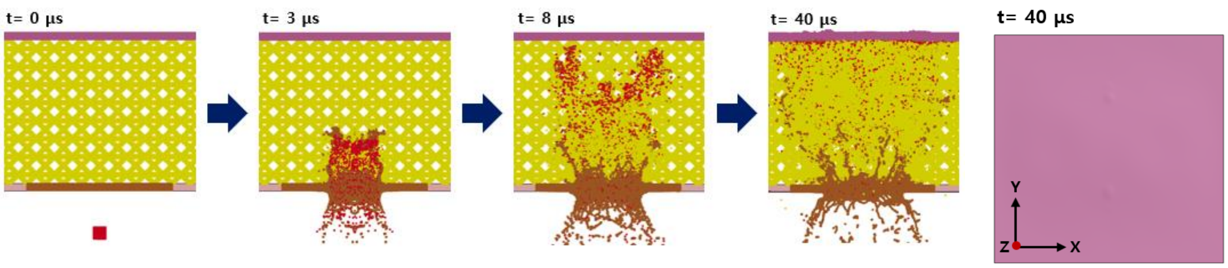

(a) Sectioned view (b) Rear view

Figure 15: HVI simulation result between Lattice Core Sandwich Panel (LCSP) and cube

DOI: 10.13009/EUCASS2023-382

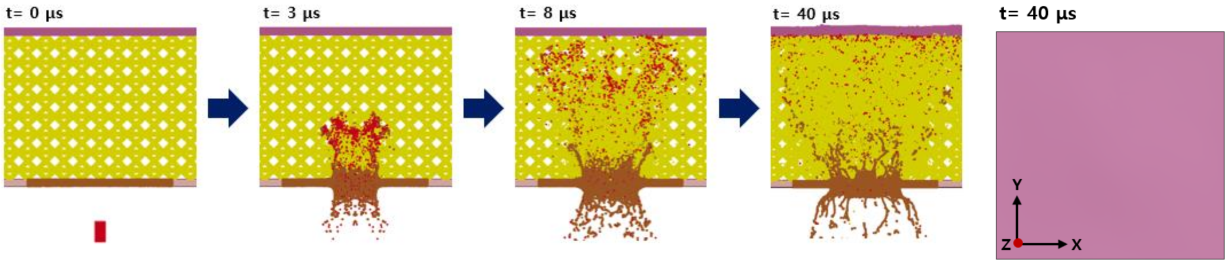

(a) Sectioned view (b) Rear view

Figure 16: HVI simulation result between Lattice Core Sandwich Panel (LCSP) and short cylinder

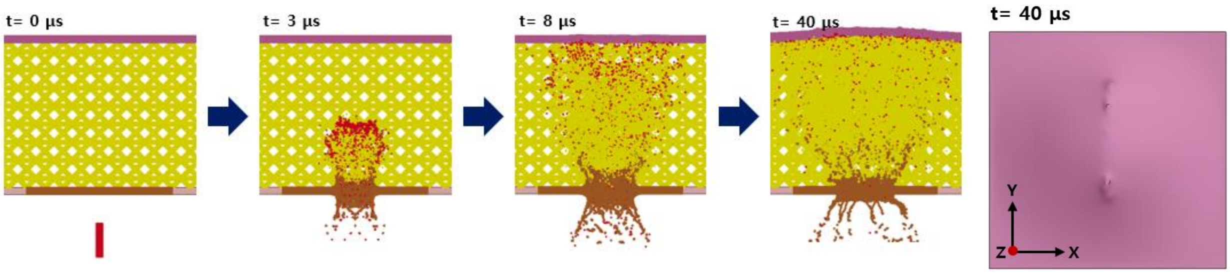

(a) Sectioned view (b) Rear view

Figure 17: HVI simulation result between Lattice Core Sandwich Panel (LCSP) and long cylinder

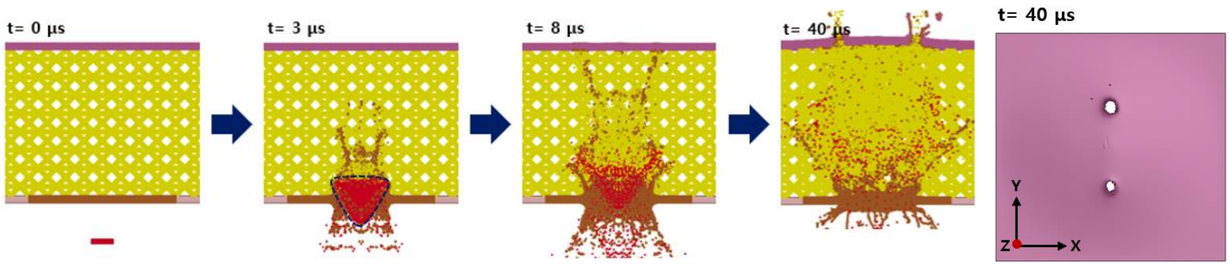

(a) Sectioned view (b) Rear view

Figure 18: HVI simulation result between Lattice Core Sandwich Panel (LCSP) and short disk

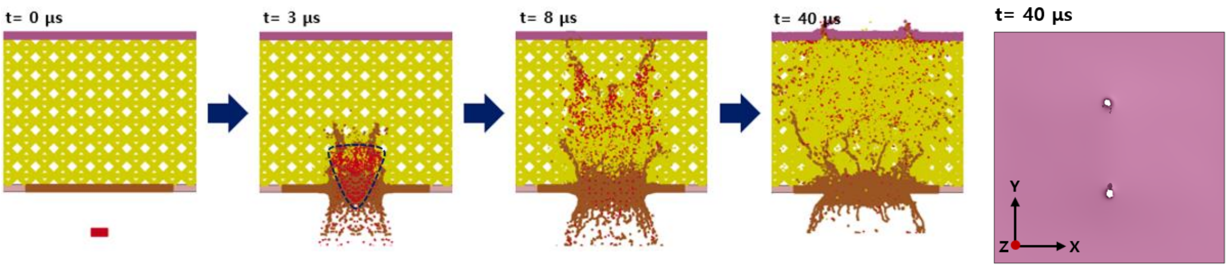

(a) Sectioned view (b) Rear view

Figure 19: HVI simulation result between Lattice Core Sandwich Panel (LCSP) and long disk

DOI: 10.13009/EUCASS2023-382

Table 4: Summary of HVI simulation results on various space objects

Shape of space objects		Result	Hole area (mm^2)
Sphere (HCSP)		Perforated	27.58
Sphere (LCSP)		Non-perforated	N/A
Cube (LCSP)		Non-perforated	N/A
Cylinder (LCSP)	Short	Non-perforated	N/A
	Long	Non-perforated	N/A
Disk (LCSP)	Short	Perforated	3.83
	Long	Perforated	1.61

4. Conclusion

In this study, hypervelocity impact simulations between space objects with various shapes and space structures, such as HCSP and LCSP, were performed using LS-DYNA, a commercial nonlinear structural dynamics analysis code. In order to compare the shielding performance of HCSP and LCSP, HVI simulations were conducted using a spherical space object. In the case of the HVI simulation using the HCSP, perforations occurred in the rear wall due to the channeling effect. In contrast, the LCSP generated only small deformations in the rear wall owing to the multishock effect. These results demonstrated that the LCSP could provide better shielding performance than the HCSP. HVI between the LCSP and space objects with various shapes were then performed to investigate the shape effects of the space objects on the shielding performance of the LCSP. Different space objects with cube, cylinder, and disk with the same mass as the mass of a sphere were considered. For LCSP sturcutre, the perforation occured only in the case with the disk shape space objects. The collision with the short disk represented the largest failure area (3.83 mm^2). Therefore, the short disk may cause a significant failure for the space structure for the HVI problem.

References

[1] ESA, Space Debris Office. 2022. Esa’s annual space environment report. Technical Report Revision 6.

[2] Cowardin, H. M. 2023. Orbital debris quarterly news. Orbital Debris Quarterly News (ODQN). 27(1).

[3] Pai, A., Divakaran, R., Anand, S., and Shenoy, S. B. 2022. Advances in the whipple shield design and development: A brief review. *Journal of Dynamic Behavior of Materials*. 1–19.

[4] Carriere, R., and Cherniaev, A. 2021. Hypervelocity impacts on satellite sandwich structures—A review of experimental findings and predictive models. *Applied Mechanics*. 2(1):25–45.

[5] Cherniaev, A., and Telichev, I. 2017. Weight-efficiency of conventional shielding systems in protecting unmanned spacecraft from orbital debris. *Journal of Spacecraft and Rockets*. 54(1):75-89.

[6] Aslebagh, R. 2021. Hypervelocity impact on satellite sandwich structures: Development of a simulation model and investigation of projectile shape and honeycomb core effects. PhD Thesis. University of Windsor.

[7] Ryan, S., Hedman, T., and Christiansen, E. L. 2009. Honeycomb vs. foam: evaluating a potential upgrade to international space station module shielding for micrometeoroids and orbital debris. NASA Johnson Space Center, Houston, NASA/TM-2009-214793.

[8] Xu, H., Yu, D., Cui, J., Shi, Z., Song, D., and Miao, C. 2023. The Hypervelocity impact behavior and energy absorption evaluation of fabric. *Polymers*. 15(6):1547.

[9] Pai, A., Divakaran, R., Anand, S., and Shenoy, S. B. 2022. Advances in the whipple shield design and development: A brief review. *Journal of Dynamic Behavior of Materials*. 1-19.

[10] Liu, P., Liu, Y., and Zhang, X. 2015. Improved shielding structure with double honeycomb cores for hyper-velocity impact. *Mechanics Research Communications*. 69:34-39.

[11] Ma, Q., Rejab, M. R. M., Siregar, J. P., and Guan, Z. 2021. A review of the recent trends on core structures and impact response of sandwich panels. *Journal of Composite Materials*. 55(18):2513-2555.

[12] Taghipoor, H., Eyvazian, A., Kumar, A. P., Hamouda, A. M., and Gobbi, M. 2020. Experimental and numerical study of lattice-core sandwich panels under low-speed impact. *Materials Today: Proceedings*, 27:1487-1492.

DOI: 10.13009/EUCASS2023-382

[13] Georges, H., Mittelstedt, C., and Becker, W. 2021. Sandwich panels with functionally graded strut-based lattice cores. *PAMM*. 21(1).
[14] Yungwirth, C. J., Wadley, H. N., O'Connor, J. H., Zakraysek, A. J., and Deshpande, V. S. 2008. Impact response of sandwich plates with a pyramidal lattice core. *International Journal of Impact Engineering*. 35(8):920-936.
[15] Wang, X., Wei, K., Wang, K., Yang, X., Qu, Z., and Fang, D. 2020. Effective thermal conductivity and heat transfer characteristics for a series of lightweight lattice core sandwich panels. *Applied Thermal Engineering*. 173.
[16] Schubert, M., and Dafnis, A. 2019. Multifunctional load-bearing aerostructures with integrated space debris protection. *In: MATEC Web of Conferences*. 304.
[17] Aslebagh, R., and Cherniaev, A. 2022. Projectile shape effects in hypervelocity impact of honeycomb-core sandwich structures. *Journal of Aerospace Engineering*. 35(1):04021112.
[18] Schonberg, W. P., and Williamsen, J. E. 2006. RCS-based ballistic limit curves for non-spherical projectiles impacting dual-wall spacecraft systems. *International Journal of Impact Engineering*, 33(1-12):763-770.
[19] Williamsen, J. E., and Evans, S. W. 2006. Predicting orbital debris shape and orientation effects on spacecraft shield ballistic limits based on characteristic length. *International Journal of Impact Engineering*. 33(1-12):862-871.
[20] Kang, P. S., Im, C. K., Youn, S. K., Lim, J. H., and Hwang, D. S. 2012. A study on the damage of satellite caused by hypervelocity impact with orbital debris. *Journal of the Korean Society for Aeronautical & Space Sciences*. 40(7):555-563.
[21] Lahiri, S. K., Bhattacharya, K., Shaw, A., and Ramachandra, L. S. 2020. A stable SPH with adaptive B-spline kernel. *Journal of Computational Physics*. 422:109761.
[22] Xu, J., Wang, J., and Souli, M. 2015. SPH and ALE formulations for sloshing tank analysis. *The International Journal of Multiphysics*. 9(3):209-224.
[23] Lee, S. S., Seo, S. W., and Min, O. K. 2003. SPH parameters for analysis of penetration phenomenon at hypervelocity impact of meteorite. *Transactions of the KSME A*, 27(10):1738–1747.
[24] Kang, P. S. 2011. A study on the honeycomb core size effect on the channeling in hypervelocity impact between orbital debris and a honeycomb sandwich panel. Master's Thesis. University of KAIST.
[25] Hallquist, J. O. 2006. LS-DYNA theory manual. Livermore software Technology corporation. 3:25-31.
[26] Cherniaev, A. 2021. Modeling of hypervelocity impact on open cell foam core sandwich panels. *International Journal of Impact Engineering*. 155:103901.
[27] Roy, S. K., Trabia, M., O'Toole, B., Hixson, R., Becker, S., Pena, M., Jennings, R., Somasoundaram, D., Matthes, M., Daykin. E., and Machorro, E. 2016. Study of hypervelocity projectile impact on thick metal plates. *Shock and Vibration*. 2016.
[28] Singh, P. K., and Kumar, M. 2022. Hypervelocity impact behavior of projectile penetration on spacecraft structure: A review. *Materials Today: Proceedings*. 62(6):3167-3171.
[29] Johnson, G. R., and Cook, W. H. 1985. Fracture characteristics of three metals subjected to various strains, strain rates, temperatures and pressures. *Engineering Fracture Mechanics*. 21(1):31-48.
[30] Kay, G. 2002. Failure modeling of titanium-6Al-4V and 2024-T3 aluminum with the Johnson-Cook material model (No. UCRL-ID-149880). Lawrence Livermore National Lab. CA (US).
[31] Akram, S., Jaffery, S. H. I., Khan, M., Fahad, M., Mubashar, A., and Ali, L. 2018. Numerical and experimental investigation of Johnson–Cook material models for aluminum (Al 6061-T6) alloy using orthogonal machining approach. *Advances in Mechanical Engineering*. 10(9).
[32] Chakrabarty, R., and Song, J. 2020. A modified Johnson-Cook material model with strain gradient plasticity consideration for numerical simulation of cold spray process. *Surface and Coatings Technology*. 397.
[33] Zhang, Y., An, F., Liao, S., Wu, C., Liu, J., and Li, Y. 2021. Study on numerical simulation methods for hypervelocity impact on large-scale complex spacecraft structures. *Aerospace*. 9(1):12.
[34] Piekutowski, A. J., 1996. Formation and description of debris clouds produced by hypervelocity impact. NASA Contractor Report 4707. Marshall Space Flight Center.
[35] Legaud, T., Le Garrec, M., Van Dorsselaer, N., and Lapoujadet, V. 2019. Improvement of satellites shielding under high velocity impact using advanced SPH method. *In 12th European LS-DYNA Conference*.
[36] Shin, H. C., and Park, J. S. 2022. Hypervelocity impact simulations considering space objects with various shapes and impact angles. *Journal of the Korean Society for Aeronautical and Space Sciences.* 50(12):829-838.